PERGAMON

International Journal of Multiphase Flow 27 (2001) 1903–1930

International Journal of Multiphase Flow

www.elsevier.com/locate/ijmulflow

Three-phase material distribution measurements in a vertical flow using gamma-densitometry tomography and electrical-impedance tomography

D.L. George [a,1], K.A. Shollenberger [a,*], J.R. Torczynski [a], T.J. O'Hern [a], S.L. Ceccio [b]

[a] *Engineering Sciences Center, Sandia National Laboratories, Albuquerque, NM 87185-0834, USA*[,2]
[b] *Department of Mechanical Engineering and Applied Mechanics, University of Michigan, Ann Arbor, MI 48109-2121, USA*

Received 5 April 2000; received in revised form 21 June 2001

Abstract

Experiments are presented in which electrical-impedance tomography (EIT) and gamma-densitometry tomography (GDT) measurements are combined to simultaneously measure the solid, liquid, and gas radial distributions in a vertical three-phase flow. The experimental testbed is a 19.05-cm diameter bubble column in which gas is injected at the bottom and exits out the top while the liquid and solid phases recirculate. The gas phase is air and the liquid phase is deionized water with added electrolytes. For the solid phase four different particle classes are investigated: 40–100 μm and 120–200 μm glass particles (2.41 g/cm^3), and 170–260 μm and 200–700 μm polystyrene particles (1.04 g/cm^3). Superficial gas velocities of 3–30 cm/s and solid volume fractions up to 0.30 are examined. For all experimental conditions investigated, the gas distribution shows only a weak dependence on both particle size and density. The average gas volume fraction as a function of superficial gas velocity can be described to within ±0.04 by a single curve. For most cases, the solid particles appear to be uniformly dispersed in the liquid.

Keywords: Gamma-densitometry tomography; Electrical-impedance tomography; Bubble column; Gas volume fraction; Multiphase flow

* Corresponding author. Tel.: +1-505-844-5823; fax: +1-505-844-8251.
E-mail address: kasholl@sandia.gov (K.A. Shollenberger).

[1] Present address: Southwest Research Institute, San Antonio, TX 78228, USA.

[2] Sandia is a multiprogram laboratory operated by Sandia Corporation, a Lockheed Martin Company, for the US Department of Energy under Contract DE-AC04-94AL85000.

0301-9322/01/$ - see front matter
PII: S0301-9322(01)00042-8

1. Introduction

The spatial distribution of materials in multiphase flows is important to many chemical and industrial processes. For example, a bubble-column reactor is used in indirect coal liquefaction in which a reactive gas is bubbled through a catalyst-laden slurry; a spatially nonuniform gas distribution within the reactor can reduce process efficiency by inducing large-scale, buoyancy-driven recirculating flows (Jackson et al., 1996). Techniques that measure the distribution of each phase in multiphase flows have the potential to improve the control of such processes. They also can be useful for validating computational models of multiphase flows (Plaskowski et al., 1995; Torczynski et al., 1997). Many techniques for measuring phase distributions are based on tomographic reconstruction methods that obtain data via probes or instruments that are placed outside the flow domain so as not to disturb the flow. Examples of these methods include gamma-densitometry tomography (GDT), electrical-impedance tomography (EIT), magnetic resonance imaging (MRI), acoustic tomography, and positron emission tomography (PET) (George et al., 1998a).

GDT and other radiation-based tomographic methods are relatively mature and can accurately measure two-phase spatial distributions (Hewitt, 1978; Kumar et al., 1995; Shollenberger et al., 1997a). Recently, an EIT system developed at Sandia National Laboratories and the University of Michigan was validated for accurate measurements of two-phase spatial distributions (O'Hern et al., 1995; Torczynski et al., 1996a; George et al., 2000). This paper documents a series of experiments in which GDT and EIT are applied simultaneously for the first time to measure time-averaged solid, liquid, and gas radial distributions in vertical three-phase flows. Combination of these two techniques is ideal because it is relatively easy to select materials such that each technique is most sensitive to only one of the phases. For example, GDT is most sensitive to the quantity of gas present because the radiation attenuation through each material scales approximately with density, and EIT is most sensitive to the quantity of conducting liquid present if both the gas and solid phases are electrically nonconducting.

The objective of this experimental study is to determine the effects that the presence of a solid phase has on material distributions in bubble-column flows. The parameters for this study include gas velocity, solids volume fraction, particle size, and particle density. This paper begins with a brief introduction to the design and theory of the GDT and EIT systems used in this study. The remaining sections of this paper describe the experimental setup, results, and conclusions.

2. Experimental techniques

2.1. Gamma-densitometry tomography

Phase distribution measurements are made with a GDT system developed at Sandia for studies of industrial-scale multiphase flows (Torczynski et al., 1996b; Shollenberger et al., 1997a). The GDT system has a 5-Ci ^{137}Cs gamma source, a sodium–iodide scintillation detector system, a computer-controlled traverse to position the source and detector, and data acquisition hardware and software. Photons emitted by the source are collimated, pass through the experimental test section, and are then collimated again prior to reaching the detector by a 3.2-mm inner-diameter

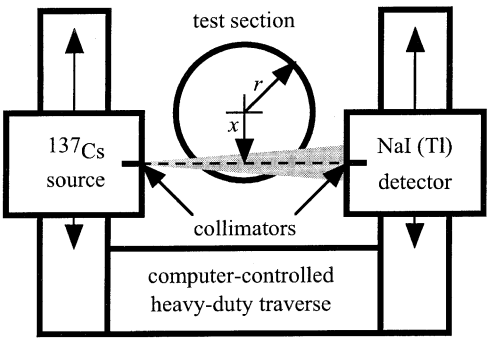

Fig. 1. Schematic diagram of GDT system applied to a circular domain showing lateral and radial coordinate systems.

lead cylinder (Fig. 1). Measurements of the number of gamma photons observed over a set period of time (intensity, I, with units of counts per second) are taken along parallel beam paths. In order to increase the stability and resolution of the observed intensities, a spectrum analyzer is used to measure the energy of all photons reaching the detector. The ^{137}Cs gamma source emits monoenergetic photons with an energy of 661.6 keV, and the measured intensities are found by a curve fit to the peak surrounding this energy level. This minimizes errors resulting from drift in energy levels because of electronics, scattered photons, and background radiation (Torczynski et al., 1997).

The changes in intensity measured between any two experiments can be related to the attenuation coefficients of the media by

$$I = I_0 \exp\left(-\sum_{i=1}^{n} \mu_i L_i \right), \tag{1}$$

where I and I_0 are the intensities with and without the attenuating media, respectively, μ_i are the attenuation coefficients (which scale with material density and are constant for a monoenergetic source), and L_i are the path lengths through each material. An attenuation coefficient averaged along each straight path ("ray") through the test section $\bar{\mu}^{\text{ray}}$ can be defined as a function of lateral location x with respect to the axis as

$$\bar{\mu}^{\text{ray}}(x) = \sum_{i=1}^{n} \mu_i \bar{\varepsilon}_i^{\text{ray}}(x), \tag{2}$$

where there are n phases and $\bar{\varepsilon}_i^{\text{ray}}$ is the ray-averaged volume fraction for each phase. For the experiments presented here, intensities are measured at each location with the column empty, $I_1(x)$, full of water, $I_2(x)$, and while the gas is flowing, $I(x)$. Using Eqs. (1) and (2), $I_1(x)$, $I_2(x)$, and $I(x)$ are related to $\bar{\mu}^{\text{ray}}(x)$ by

$$\bar{\mu}^{\text{ray}}(x) = \mu_1 \frac{\ln\left[I(x)/I_2(x)\right]}{\ln\left[I_1(x)/I_2(x)\right]} - \mu_2 \frac{\ln\left[I(x)/I_1(x)\right]}{\ln\left[I_1(x)/I_2(x)\right]}. \tag{3}$$

Finally, $\bar{\mu}^{\text{ray}}(x)$ is normalized with respect to the gas and liquid phase attenuation coefficients, μ_1 and μ_2, respectively, to obtain

$$\psi(x) = \frac{\bar{\mu}^{\text{ray}}(x) - \mu_1}{\mu_2 - \mu_1} = \frac{\ln[I(x)/I_1(x)]}{\ln[I_2(x)/I_1(x)]}. \tag{4}$$

The normalized ray-averaged attenuation coefficient $\psi(x)$ varies from 0 to 1 as the multiphase mixture varies from pure gas to pure liquid. Thus, attenuation by the testbed walls is subtracted from the raw data; then a time-averaged, normalized radial attenuation distribution,

$$f_\mu(r) = \frac{\mu(r) - \mu_1}{\mu_2 - \mu_1}, \tag{5}$$

is reconstructed from the Abel transform of $\psi(x)$ (Vest, 1985) with the assumption of an axisymmetric phase distribution. In Eq. (5), $\mu(r)$ is related to material volume fractions in an analogous fashion to $\bar{\mu}^{\text{ray}}(x)$ as

$$\mu(r) = \sum_{i=1}^{n} \mu_i \varepsilon_i(r), \tag{6}$$

where $\varepsilon_i(r)$ is the volume fraction of each phase at each radial location.

The axisymmetric attenuation and phase distributions are modeled as fourth-order polynomials using only even powers of r as shown for $f_\mu(r)$:

$$1 - f_\mu(r) = a_0 + a_1\left(\frac{r}{R}\right)^2 + a_2\left(\frac{r}{R}\right)^4, \tag{7}$$

where R is the radius of the circular domain. The choice of the quartic function is justified by the work of previous researchers who measured similar profiles using point probe techniques (Shah and Deckwer, 1983; Torczynski et al., 1997). Two special cases of interest arise when phase 1 is a gas (μ_1 is negligible) and: (1) there are only two phases ($n = 2$), or (2) there are three phases ($n = 3$) and the remaining two phases have the same attenuation coefficient ($\mu_2 = \mu_3$). Then the following relationships can be derived from Eqs. (2)–(6) between gas volume fraction, $\bar{\varepsilon}_{\text{G}}^{\text{ray}}(x)$ or $\varepsilon_{\text{G}}(r)$, the normalized ray-averaged attenuation coefficient, $\psi(x)$, and the normalized attenuation coefficient, $f_\mu(r)$:

$$\bar{\varepsilon}_{\text{G}}^{\text{ray}}(x) = 1 - \psi(x) \quad \text{and} \quad \varepsilon_{\text{G}}(r) = 1 - f_\mu(r). \tag{8}$$

Thus, for these two cases, gas volume fraction can be measured directly with GDT. For three-phase flows if the attenuation coefficients are significantly different for each phase, additional information is required to resolve all three-phase-volume-fraction profiles.

2.2. Electrical-impedance tomography

Additional phase distribution measurements are made with an EIT system that was developed collaboratively by Sandia National Laboratories (Torczynski et al., 1997; George et al., 1998b) and the University of Michigan and has been calibrated for two-phase measurements using the Sandia GDT system. Details of the design and implementation of this system are described in detail by George et al. (2000) and are summarized here. The EIT system consists of the following components:

- an electrode array;
- a signal generator;

- a voltage-controlled current source;
- multiplexers connecting the electrode array to the current source, ground, and measurement electronics;
- an instrumentation amplifier and phase-sensitive demodulators;
- a low-pass filter to eliminate high-frequency components from the demodulated signals;
- a data acquisition card.

The data acquisition card contains an analog-to-digital converter that measures the DC signal components and a digital controller that can be used to select electrodes for current injection, ground, and measurement. The card also acts as an interface to a PC that operates the entire system.

During operation the EIT system injects a controlled current through one electrode, "sinks" a second electrode to ground, and measures voltages at all electrodes relative to ground as shown schematically in Fig. 2. A "projection set" is defined as measurements at all N electrodes for all distinct injection and ground combinations, for a total of $N^2(N-1)/2$ voltage measurements. This is a factor of N greater than the number of independent pieces of information, $N(N-1)/2$; the extra information is used to reduce the impact of noise on the reconstructions.

The domain is excited with a 50-kHz AC electric field. The voltage signal from each electrode passes through an amplifier to a pair of phase-sensitive demodulators that separate the measured signal into two components: one demodulator produces the component in phase with the EIT carrier signal, and the other yields the quadrature component out of phase with the carrier by 90°. Because the demodulators multiply two 50-kHz signals together (the measured voltage and the carrier or quadrature reference signal), their outputs consist of a 100-kHz sine wave superimposed on a DC component. The sine wave is removed by the low-pass filter, yielding the DC component, which is proportional to the carrier or quadrature component of the measured voltage.

The electrode array discussed in this paper and shown in Fig. 3 was fabricated for use both in validation tests and in experiments conducted in the transparent bubble column (Section 3.1). The 16 electrodes were made from stainless steel strips 0.64 cm wide, 7.62 cm high, and 76 μm thick.

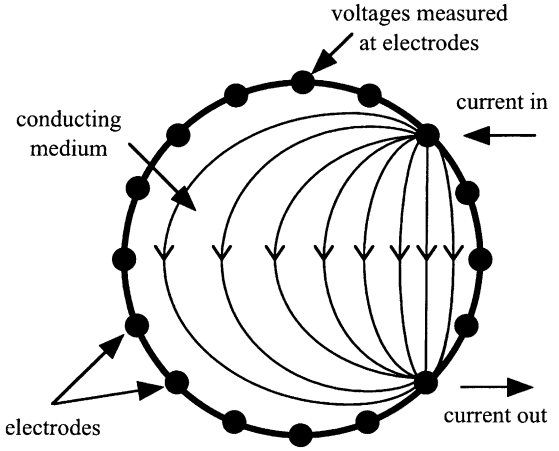

Fig. 2. Conceptual diagram of an EIT system applied to a circular domain.

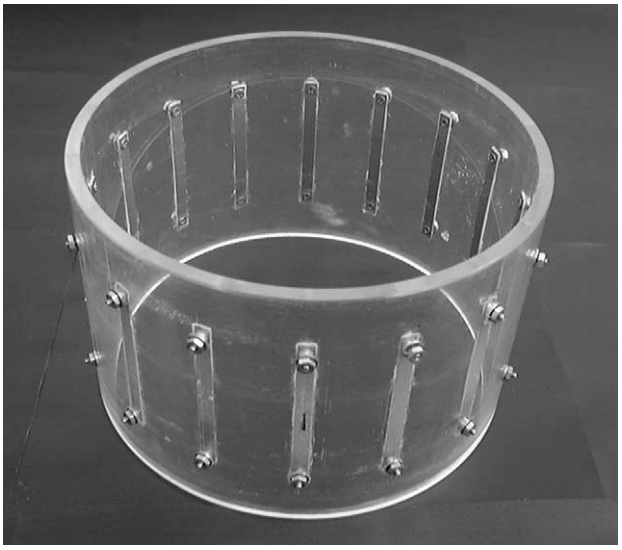

Fig. 3. EIT strip electrode array. The bottom scale is in inches.

These were mounted at equal azimuthal intervals in a Lucite cylinder with an inner diameter of 19.05 cm, a wall thickness of 0.64 cm, and a height of 12.7 cm. For 16 electrodes, the acquisition time for each voltage projection set is either 0.5 s using integrated circuit counters or 1.5 s using a software-controlled command option. Validation tests presented in George et al. (2000) demonstrated that the choice of mode has little impact on reconstruction accuracy.

In EIT, the measurements at the domain boundary are used to reconstruct the impedance distribution within the domain and to infer the phase distribution. For AC electrical conduction with a field frequency f in a domain $\mathbf{D}$ with a (purely resistive) electrical conductivity σ, the electric potential V is given by

$$\nabla \cdot \sigma \nabla V = 0. \tag{9}$$

Eq. (9) assumes that no charge sources or sinks are present in $\mathbf{D}$. Eq. (9) also assumes that capacitive effects are negligible, which yields the constraint $\sigma >> 2\pi f \tilde{\varepsilon}\varepsilon_0$, where $\tilde{\varepsilon}$ is the dielectric constant for the medium and $\varepsilon_0 = 8.85 \times 10^{-12}$ F/m is the permittivity of a vacuum (Somersalo et al., 1992). The boundary conditions on $\mathbf{D}$ are given by

$$\mathbf{n} \cdot \sigma \nabla V + j = 0, \tag{10}$$

where $\mathbf{n}$ is the unit normal vector outward from the domain boundary, and j is the charge flux on the boundary. Multiple measurements of j and V at the boundary are used to reconstruct the conductivity distribution within $\mathbf{D}$ that yields the measured boundary conditions. More information on EIT theory and the development of EIT systems for the study of multiphase flows may be found in Dickin et al. (1993), Jones et al. (1992, 1993, 1994), and Ceccio and George (1996).

The reconstruction algorithm used with the Sandia EIT system has been described in detail by Torczynski et al. (1996a, 1997) and is based on the YWT method described by Yorkey et al. (1987). This algorithm is summarized here. The medium is surrounded by an insulating boundary

through which current is injected or withdrawn at discrete electrodes. A finite-element method (FEM) representation is generated for the voltage equation, identical in form to the steady-state heat-conduction equation. Unlike most FEMs, the conductivity is not represented by a piecewise-constant function that is discontinuous at element boundaries. Instead, the electrical conductivity is represented as a global function of position and of one or more conductivity parameters. Current flow is specified at the electrodes for the boundary conditions such that the net current into and out of the domain is zero.

The finite-element equations generated from Eqs. (9) and (10) are solved to find both the predicted voltages at the electrodes and the derivatives of the electrode voltages with respect to the conductivity parameters. Subsequently, the conductivity parameters are adjusted by a Newton–Raphson algorithm to minimize the least-squares difference between the computed and experimental electrode voltages at the non-current-bearing electrodes. Since no voltages are prescribed in the computational boundary conditions, the computed voltage solution of Eq. (9) is unique only to within an arbitrary additive constant. The value of the additive constant is determined during the least-squares minimization process (see George et al., 2000). The model used to implement this approach considers cylindrical domains within which the conductivity varies only radially but the voltage fields vary three-dimensionally to reflect the finite axial extent of the electrodes. The calculated conductivity field is represented as a global function of radial position and of conductivity parameters. The following representation of a quartic radial conductivity profile is chosen:

$$\frac{\sigma(\tilde{r})}{\sigma_{\mathrm{L}}} = \frac{1 + C_1\left(2\tilde{r}^2 - 1\right) + C_2\left(1 - 6\tilde{r}^2 + 6\tilde{r}^4\right)}{C_0}, \tag{11}$$

where σ_{L} is the liquid phase conductivity, C_1 and C_2 are the conductivity shape parameters, C_0 is a scale parameter, $\tilde{r} = r/R$, r is the radial coordinate, and R is the radius of the circular domain. The particular form of Eq. (11) has several advantages. Eq. (11) can represent any symmetric quartic profile that is physically allowable (positive at all radii) so long as the parameters are appropriately chosen. The C_0 dependence ensures that the cross-sectionally averaged conductivity is positive so long as C_0 is positive. Moreover, the voltages for arbitrary values of C_0 are trivially obtained by scaling the voltages for $C_0 = 1$. It is straightforward to show that physically acceptable C_1 and C_2 values occupy a closed, convex region in the C_1–C_2 plane. Moreover, the three basis functions $\{1, 2\tilde{r}^2 - 1, 1 - 6\tilde{r}^2 + 6\tilde{r}^4\}$ are orthogonal with respect to cross-sectional averaging. Enforcing $C_2 = 0$ allows the importance of the quartic term to be determined, and enforcing $C_1 = 0$ and $C_2 = 0$ allows the importance of the quadratic term to be determined.

A constitutive model is required to relate the electrical conductivity to the conducting and insulating phase volume fractions. When the continuous liquid phase is the only conducting phase, the Maxwell–Hewitt relation (Maxwell, 1881; Hewitt, 1978) can be used to relate the mixture conductivity, σ, and the liquid conductivity, σ_{L}, to the insulating phase volume fraction, ε_{I}:

$$\frac{\sigma}{\sigma_{\mathrm{L}}} = E(\varepsilon_{\mathrm{I}}, \alpha), \quad E(\xi, \eta) \equiv \frac{1 - \xi}{1 + \eta\xi}, \tag{12}$$

where the functional form of E is defined above. This equation is a good approximation for the dispersed media considered here in which the size of inclusions is much less than any characteristic geometric length, as verified by the analysis in George et al. (2000). In Eq. (12), the parameter $\alpha = 1/2$ for three-dimensional inclusions of an insulating phase dispersed in a conducting phase (e.g., bubbles or insulating solid particles in salt water). An analogous relation can be derived for the somewhat artificial case of two-dimensional insulating inclusions dispersed in a conducting phase (e.g., parallel insulating posts in salt water) by using $\alpha = 1$ in Eq. (12). Validation experiments in two-phase bubble-column flows by George et al. (2000) showed that $\alpha = 3/5$ provided the best agreement between the EIT and GDT profile data. The parameter, α, may lie between the two extreme cases because of the vertical motion or axial elongation of the bubbles during each measurement period or simply because the Maxwell–Hewitt relation is heuristic rather than rigorous. Interestingly, the value of $\alpha = 3/5$ brings the Maxwell–Hewitt relation into better agreement with the FEM simulations by George et al. (2000) of the effective conductivity of insulating inclusions. Thus, $\alpha = 3/5$ is used for all of the results presented here.

2.3. Combined GDT/EIT technique

The previously described GDT and EIT techniques can be combined to make three-phase material distribution measurements. Three relations are used to determine the radial variations of the gas, liquid, and solid volume fractions ($\varepsilon_G(r)$, $\varepsilon_L(r)$, and $\varepsilon_S(r)$, respectively): the normalized gamma attenuation, $f_\mu(r)$, the normalized electrical conductivity, $\sigma(r)/\sigma_L$, and the total volume relationship:

$$\varepsilon_G(r) + \varepsilon_L(r) + \varepsilon_S(r) = 1. \tag{13}$$

The only additional information needed to calculate $\varepsilon_G(r)$, $\varepsilon_L(r)$, and $\varepsilon_S(r)$ are four physical properties known a priori: the phase attenuation coefficients, μ_S, μ_L, and μ_G, listed in Table 1 and the liquid conductivity, σ_L, measured with the EIT system. For the bubble-column flow investigated in this paper, two different ways of applying the Maxwell–Hewitt relation (Eq. (12)) are considered.

For the case where the quantity $\varepsilon_I(r)$ in Eq. (13) is set equivalent to the total insulating phase fractions, $\varepsilon_I(r) = \varepsilon_G(r) + \varepsilon_S(r) = 1 - \varepsilon_L(r)$, $\varepsilon_L(r)$ can be solved for directly from Eq. (12) as

$$\varepsilon_L(r) = \frac{(1+\alpha)\sigma(r)/\sigma_L}{1 + \alpha\sigma(r)/\sigma_L}. \tag{14}$$

Calculation of the gas volume fraction from $\varepsilon_L(r)$ and GDT data is derived from Eqs. (5) and (6) as

Table 1
Physical properties of the materials used in the three-phase experiments

Material	ρ (g/cm^3)	μ (cm^{-1})	σ (μS/cm)	$\tilde{\varepsilon}\varepsilon_0$ (μF/cm)
Polystyrene	1.04	0.0866	$<10^{-10}$	2.3×10^{-7}
Glass	2.41	0.209	5.9×10^{-11}	$\approx 5 \times 10^{-7}$
Water/$NaNO_3$	0.997	0.0856	242–243	$\approx 7 \times 10^{-6}$
Air	0.00106	0.0000819	$\approx 10^{-10}$	8.86×10^{-8}

$$\varepsilon_G(r) = 1 - \left(\frac{\mu_L - \mu_G}{\mu_S - \mu_G}\right) f_\mu(r) - \left(\frac{\mu_S - \mu_L}{\mu_S - \mu_G}\right) \varepsilon_L(r). \tag{15}$$

Finally, $\varepsilon_S(r)$ is calculated using Eq. (13).

The second implementation of the Maxwell–Hewitt relation is more complicated. As discussed in George et al. (2000), the Maxwell–Hewitt relation can be modified to represent a bimodal distribution of "particle" sizes (i.e., large bubbles and small solid particles) by treating the three-phase flow as gas bubbles within a liquid–solid mixture. In this case the modified Maxwell–Hewitt relation is applied recursively, first to the solid particles in the liquid phase, then to the gas in the liquid–solid mixture. The following relation replaces Eq. (14):

$$\frac{\sigma(r)}{\sigma_L} = E[\varepsilon_G(r), \alpha] E\left[\frac{\varepsilon_S(r)}{\varepsilon_S(r) + \varepsilon_L(r)}, \alpha\right]. \tag{16}$$

Eq. (16) can no longer be solved directly for $\varepsilon_L(r)$, so Eqs. (13), (15) and (16) are solved simultaneously to determine each volume fraction profile. A closed-form solution is given below:

$$a(r) = 1 + \left[\left(\frac{\mu_S - \mu_L}{\mu_S - \mu_G}\right)\alpha - \left(\frac{\mu_L - \mu_G}{\mu_S - \mu_G}\right)\alpha^2\right]\frac{\sigma(r)}{\sigma_L},$$

$$b(r) = -2 + \left(\frac{\mu_L - \mu_G}{\mu_S - \mu_G}\right) f_\mu(r) + \left\{\left(\frac{\mu_S - \mu_L}{\mu_S - \mu_G}\right) - \alpha + \left(\frac{\mu_L - \mu_G}{\mu_S - \mu_G}\right)\left[1 - f_\mu(r)\right]\alpha^2\right\}\frac{\sigma(r)}{\sigma_L},$$

$$c(r) = 1 - \left(\frac{\mu_L - \mu_G}{\mu_S - \mu_G}\right) f_\mu(r) + \left\{-\left(\frac{\mu_S - \mu_L}{\mu_S - \mu_G}\right) + \left(\frac{\mu_L - \mu_G}{\mu_S - \mu_G}\right)\left[1 - f_\mu(r)\right]\alpha\right\}\frac{\sigma(r)}{\sigma_L},$$

$$\varepsilon_G(r) = \frac{-b(r) + \sqrt{b(r)^2 - 4a(r)c(r)}}{2a(r)}, \tag{17}$$

$$\varepsilon_L(r) = \left(\frac{\mu_S - \mu_G}{\mu_S - \mu_L}\right) - \left(\frac{\mu_L - \mu_G}{\mu_S - \mu_L}\right) f_\mu(r) - \left(\frac{\mu_S - \mu_G}{\mu_S - \mu_L}\right)\varepsilon_G(r). \tag{18}$$

Once again $\varepsilon_S(r)$ is calculated using Eq. (13). Because this modified Maxwell–Hewitt relation is more appropriate for the "bimodal" mixture (small particles and large bubbles) found in these experiments, it was used to calculate all the profiles in this paper. However, this treatment has only a modest effect on the calculated phase volume fractions at their highest values and is included mainly to show that this issue has been considered.

3. Experimental setup

3.1. Testbed setup

The three-phase experiments are conducted in a vertical bubble column, shown schematically in Fig. 4. The column is constructed of transparent Lexan with an inside diameter, D, of 19.05 cm and a wall thickness of 0.64 cm. It is built from interchangeable sections so that different diagnostics can be placed in the column. In each three-phase experiment, the column is initially filled

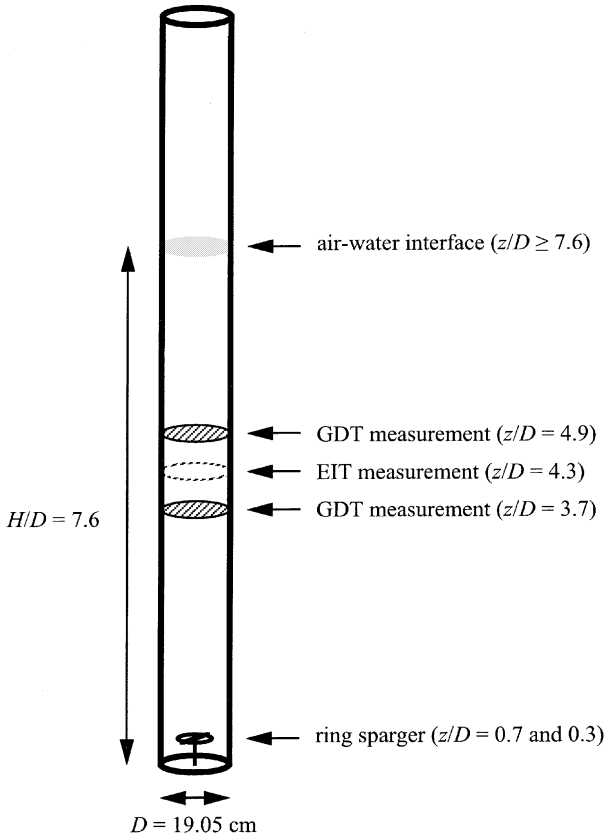

Fig. 4. Schematic diagram of Lexan bubble column (19-cm i.d.) used in three-phase flow experiments showing measurement locations.

with water and solids to a depth, H, of 144.8 cm, for a height-to-diameter ratio of $H/D = 7.6$. The 16 strip electrodes are centered on a plane $z = 82.0$ cm above the base ($z/D = 4.3$), completely immersing the region of EIT sensitivity. GDT scans are taken on two source-detector planes located at $z = 70.6$ and 93.4 cm above the column base ($z/D = 3.7$ and 4.9). These positions above and below the midplane of the EIT electrode ring are chosen to prevent obstruction by the electrodes, the cables exterior to the electrode ring, and the O-ring collars that join the electrode ring to the remainder of the column. These measurement locations also ensure that there are minimal changes in phase volume fractions in the axial direction across the EIT measurement region.

A ring sparger is used to introduce dry air into the flow near the bottom of the column. The sparger is a hollow stainless steel toroid with a 10.16-cm centerline diameter, a tube-inner diameter of 0.95 cm, and 10 evenly spaced holes of 0.16-cm diameter. The sparger holes are pointed towards the bottom of the column to loft the solids from the column floor. In the experiments with the 200–700 μm polystyrene particles, the sparger is located approximately 13 cm above the base of the column. To improve the lofting efficiency of the sparger for the denser glass spheres, the sparger is lowered to a position 6 cm above the base of the column. All tests are conducted at

ambient pressure. Three cartridge heaters along the height of the column are used to counteract evaporative cooling by maintaining a constant temperature. The liquid temperature is held constant to within ±0.4°C during experiments, which limits conductivity variations induced by temperature variations to ±0.6%.

3.2. Material properties

The material properties of the phases used in these experiments are presented in Table 1. Deionized water is used as the liquid phase, with controlled amounts of sodium nitrate added to increase the conductivity. At a frequency of $f = 50$ kHz, the resistive component of the impedance dominates for air–water flows if the liquid conductivity $\sigma_L >> 2\pi f \tilde{\varepsilon}_L \varepsilon_0 \approx 2$ μS/cm where $\tilde{\varepsilon}_L \approx 80$ is the dielectric constant for water and $\varepsilon_0 = 8.85 \times 10^{-12}$ F/m is the permittivity of a vacuum (Somersalo et al., 1992). In this work, the initial DC conductivity of the aqueous sodium nitrate solution, measured before the first test at each solid loading, is $\sigma_L = 261 \pm 19$ μS/cm, which ensures that the above criterion was met. The attenuation coefficient of glass (see Table 1) is measured with the GDT system itself to account for unknown quantities of impurities (Shollenberger et al., 1997b), whereas the attenuation coefficients of polystyrene, air, and water are obtained from the literature (Lamarsh, 1983; Thoraeus, 1965). The density of air ρ_G is calculated assuming that it is an ideal gas at a pressure determined by the depth of the EIT measurement plane and at the controlled temperature. The value of the gas density varies by less than 2.5% over the extent of the GDT and EIT measurement planes ($L/D = 1.2$), so the gas attenuation coefficient changes by a similar amount. These changes are assumed to be negligible for the phase volume fraction calculations because the gas attenuation coefficient is three orders of magnitude less than the attenuation coefficient of the liquid and solid phases.

To determine whether density and size distribution of the solid particles affect the behavior of the other phases, experiments are performed with four different types of particles. The particles are chosen so that the effects of size and density could be observed separately: polystyrene particles, with a density of 1.04 g/cm^3 and with nominal diameters of 200 and 450 μm; and glass particles, with a density of 2.41 g/cm^3 and with nominal diameters of 70 and 150 μm. The solid densities are measured by a volumetric method.

Plots of the particle size distributions, in terms of number percentage and volume percentage, measured using a Mie-scattering technique are shown in Fig. 5. The size distribution of the "large" polystyrene particles is seen to be broadest by far, with 98% of the volume of solids consisting of particles with diameters in the range of 200–700 μm with a mean of 450 μm. The "small" glass particles are seen to have diameters generally in the range of 40–100 μm with a mean of 70 μm. The "medium" glass and polystyrene particles are identified by their respective manufacturers as nominally 200 μm in diameter but have notably different distributions: 120–200 μm with a mean of 150 μm for the glass spheres, 170–260 μm with a mean of 200 μm for the polystyrene. From photographs of the particles, it is apparent that some of the small glass particles are decidedly aspherical: most are globular, but some elongated particles and shards are present. By comparison, the other particles are almost uniformly spherical.

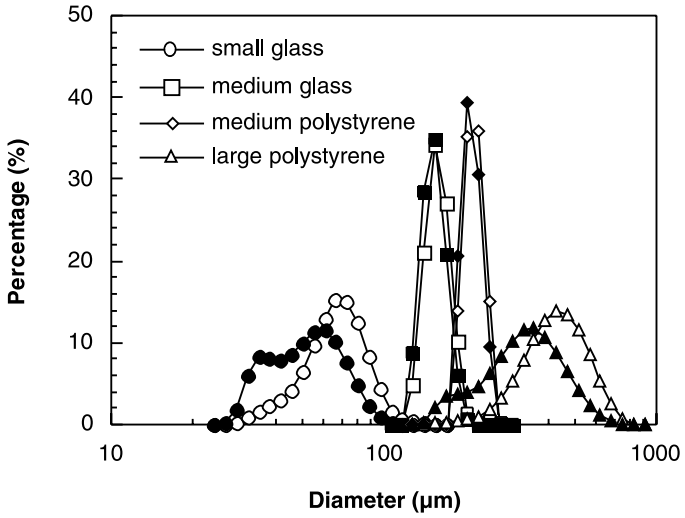

Fig. 5. Size distribution of glass (density 2.41 g/cm^3) and polystyrene (density 1.04 g/cm^3) particles. Open symbols are volume percent; closed symbols are number percent.

3.3. Experimental procedure

The polystyrene particles are washed and rinsed repeatedly to minimize the amount of soluble contamination carried by the solids into the liquid before the first set of three-phase experiments. Despite these efforts, noticeable amounts of opaque coating material are transferred from the polystyrene particles into the liquid. The coating material acts as a surfactant, as evidenced by foam appearing at the top of the liquid column during gas flow. Electrolytes present in the coating material also alter the liquid conductivity over the course of experiments. To compensate for the effect of the contaminants, a standard procedure of using the EIT system itself to measure the baseline liquid conductivity between tests is followed. The glass spheres also shed opaque material into the liquid during experiments. Although the glass particles are not washed before tests, the conductive effects of their contaminant are much less than that of the polystyrene, suggesting that a different coating is involved or perhaps that the "contaminant" is very small shards of broken particles. Again, baseline EIT conductivity measurements taken between flow conditions are used to compensate.

Table 2 lists the combinations of solid materials, solids loading, and superficial gas velocities at which measurements of phase distributions are made. The superficial gas velocity, U_G, is defined as the average velocity the gas would have if it moved through the column alone: $U_G = \dot{m}_G/(\rho_G A)$, where $\dot{m}_G$ is the gas mass flow rate, ρ_G is the gas density, and A is the cross-sectional column area. Experiments are divided into subsets, each involving one nominal slurry concentration, $\bar{\varepsilon}_S^{nom}$, defined as the ratio of the total volume of solid particles to the combined volume of the liquid and solid particles. Slurry concentrations up to $\bar{\varepsilon}_S^{nom} = 0.30$ are included in the tests with large polystyrene particles; concentrations for the other solids are limited to $\bar{\varepsilon}_S^{nom} = 0.15$, the highest loading of glass particles that can be completely lofted for these gas velocities. To obtain the desired slurry concentrations for each subset, the total mass of required particles is computed from the reference

Table 2
Average gas volume fractions for three-phase experiments from the EIT/GDT system

Particle type	U_G (cm/s)							
	$\bar{\epsilon}_S^{nom}$	2.9	5.8	8.8	11.7	17.5	23.4	29.2
40–100 μm glass (small)	0.00			0.181	0.214	0.263	0.304	
	0.05	a	a	0.141	0.185	0.242	0.283	
	0.10	a	a	0.144	0.197	0.244	0.282	
	0.15	a	a	a	0.168	0.223	0.268	
120–200 μm glass (medium)	0.00					0.246	0.290	0.321
	0.05	a	a	a	a	0.245	0.280	0.317
	0.10	a	a	a	a	0.229	0.277	0.307
	0.15	a	a	a	a	0.231	0.267	0.298
170–260 μm polystyrene (medium)	0.00	0.090	0.149	0.193	0.220	0.256	0.288	
	0.05	0.101	0.166	0.199	0.221	0.256	0.283	
	0.10	0.106	0.177	0.216	0.243	0.279	0.308	
	0.15	f	0.171	0.213	0.242	0.275	0.298	
200–700 μm polystyrene (large)	0.00	0.089	0.147	0.190	0.222			
	0.05	0.088	0.143	0.179	0.207			
	0.10	0.089	0.147	0.180	0.210			
	0.22	0.090	0.152	0.181	0.207			
	0.30	f	0.149	0.189	0.215			
Deionized water	0.00	0.075	0.117	0.137	0.167	0.213	0.249	

a = air flow rate inadequate to loft all solids; f = foam from surfactant in particle coating expanded to top of column.

volume (41.26 L, based upon a depth of $H = 144.8$ cm) and the known density of the solid material.

The downward flow of air from the sparger is sufficient to loft all of the solids from the bottom and produce a three-phase flow throughout the column in each successful test. No measurements are made for certain combinations of gas flow rate and solid volume fraction, as indicated in Table 2, because an appreciable amount of solid particles remains at the bottom of the column under these conditions. Lofting efficiency is influenced both by particle density and to some extent by particle diameter. It should be noted that cases of "0%" nominal slurry concentration employ water in which solids previously added are removed for the test, leaving coating material in the water. This is necessary to ensure that the surface tension is the same for all experiments, both with and without solids present. Table 2 also notes flow conditions that could not be completed because of excessive surfactant foam above the solid–liquid mixture.

Profile measurements at each flow condition consist of a GDT scan at the lower scan plane, followed by an EIT scan, followed by a second GDT scan at the upper plane. After the profile measurements are completed at each condition, gas flow is terminated, and the solids are allowed to settle well beyond the EIT measurement region to the bottom of the column. This settling process requires 15–60 minutes, depending upon the amount and type of solids present. Following the settling period, EIT is applied again to measure changes in the baseline conductivity of the liquid. The values of liquid conductivity measured before and after each set of flow conditions are averaged to determine the conductivity during flow.

The information from the pair of GDT scans is averaged and combined with the EIT data to determine the radial volume fraction profiles at the EIT electrode plane. Averaging of the two GDT scans assumes that the changes in phase volume fractions vary linearly with vertical location between the measurement planes, which is a reasonable approximation given the small changes measured. The two GDT scans also verify that the presence of the EIT electrode ring does not significantly influence the flow. Each GDT scan includes data acquisitions for 60 s along 19 parallel beam paths that span the column from one side to the other at 2.0-cm intervals. Thus, GDT reconstructions represent averages over a period of about 20 min. Repeated checks of the side-to-side symmetry of the measured attenuation profiles have demonstrated that the axisymmetric assumption is valid over the long acquisition time scales of GDT. For the first experiments with large polystyrene particles, 25 EIT projection sets are acquired in the fast mode (integrated circuit counters, 0.5 s per EIT projection set) during each flow condition over a period of about 20 s and averaged to yield voltage data for reconstructions. After these experiments, uncertainty analyses of the quartic EIT reconstruction algorithm showed that a total of 100 projection sets should be collected and averaged for the remaining tests. A second change is that the data acquisition is now performed in the slow mode (software controlled, 1.5 s per EIT projection set). As a result, EIT reconstructions for the remaining tests represent averages over a period of 150 s.

3.4. Sources of uncertainty

There are several sources of uncertainty that must be accounted for and minimized when making gamma-densitometry measurements. These are addressed in detail in a previous paper (Shollenberger et al., 1997a), and some of the results of the uncertainty analysis are repeated here. First, the densitometry measurements are validated by confirming that they accurately measure the cross-sectional dimension L of the column. The uncertainty $|\mathrm{d}L|$ for this measurement due to radiation fluctuations for each ray-averaged data point can be calculated from Shollenberger et al. (1997a) as

$$|\mathrm{d}L| = \frac{1}{\mu}\sqrt{\frac{1}{N_{\mathrm{full}}} + \frac{1}{N_{\mathrm{empty}}}}, \tag{19}$$

where L is the length of the domain, μ is the attenuation coefficient of water, and N_{full} and N_{empty} are the number of photons counted with the vessel full of water and empty, respectively. For these experiments, a fixed time period is chosen, so the total number of photons counted is directly proportional to the intensity, which depends on the material density along that ray. At the centerline of the column where $L = 19.05$ cm, $N_{\mathrm{full}} = 198,000 \pm 1000$ counts and $N_{\mathrm{empty}} = 998,000 \pm 4000$. At the measurement location closest to the edge of the column where $L = 6.24$ cm, $N_{\mathrm{full}} = 490,000 \pm 2500$ counts and $N_{\mathrm{empty}} = 820,000 \pm 4000$. Using the attenuation coefficient for water in Table 1, the uncertainty in the path length measurement is ± 0.03 cm at the center and ± 0.02 cm at the edge of the column. This measurement is repeated 10 times throughout the course of these experiments to verify that the uncertainty remains within the range stated above.

For measurements of the normalized ray-averaged attenuation coefficient, $\psi(x)$, the uncertainty $|\mathrm{d}\psi(x)|$ due to radiation fluctuations for each data point can be calculated from Shollenberger et al. (1997a) as

$$|\mathrm{d}\psi(x)| = \frac{1}{\mu L}\sqrt{\frac{2\left[\psi(x)^2 - \psi(x) + 1\right]}{N_{\mathrm{full}}^{1-\psi(x)} N_{\mathrm{empty}}^{\psi(x)}}}. \tag{20}$$

At the centerline, the estimated uncertainty decreases slightly from ± 0.002 to ± 0.001 as $\psi(x)$ increases. Near the column wall, the uncertainty is higher due to the reduced contrast near the wall and decreases slightly from ± 0.004 to ± 0.003 as $\psi(x)$ increases.

Fig. 6 shows an example of GDT measurements both above and below the EIT measurement plane for the large polystyrene particles at a nominal slurry concentration, $\bar{\varepsilon}_{\mathrm{S}}^{\mathrm{nom}}$, of 0.10 for a range of superficial gas flow rates. For each flow rate, a quartic fit to the data both above and below the EIT measurement plane is plotted on this figure. For this case, the standard deviation for the data points to the quartic fit is ± 0.006. For all of the cases with water and polystyrene particles, for which minimal stratification of the flow is expected, the standard deviation is always less than ± 0.01. For cases where glass particles are used and a small degree of stratification is detected, the standard deviation increases slightly to ± 0.02 for $\bar{\varepsilon}_{\mathrm{S}}^{\mathrm{nom}} = 0.15$. The increase in the standard deviation is principally due to the stratification and the fact that a single curve is used to fit data both above and below the EIT measurement plane.

Up to this point, only errors for a steady-state measurement have been discussed. Additional uncertainties are introduced because of the unsteady flow in the bubble column, namely a continuous fluctuation of gas into and out of the domain being measured. In general, it is expected that these fluctuations increase the standard deviation, which probably accounts for fact that the

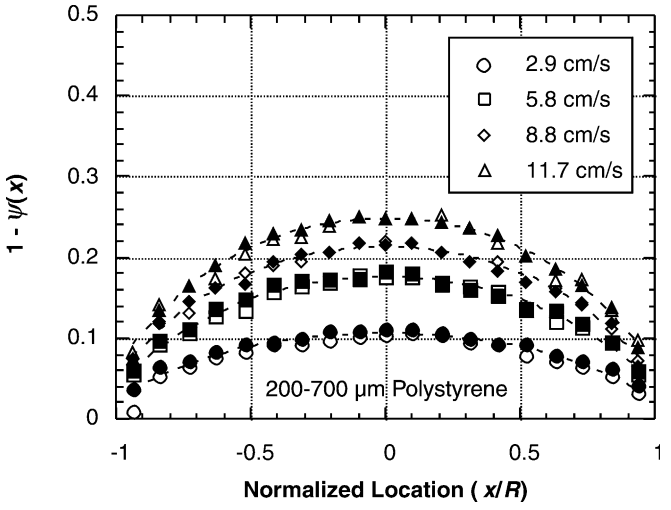

Fig. 6. Ray-averaged normalized attenuation, $\psi(x)$, as a function of normalized location and superficial gas velocity. Open and closed symbols are data collected below and above the EIT measurement plane, respectively. The solid phase is 200–700 μm polystyrene particles at a nominal slurry concentration of 0.10.

measured standard deviation is larger than the predicted value noted above. In addition, according to the equations given for calculating $\psi(x)$, the average of the natural logarithm of the count rate is needed. However, the average count rate is what is actually measured, and its natural logarithm is subsequently taken. This results in a systematic overestimation or bias from its actual value. In order to estimate the magnitude of this effect, a simple model for two-phase flow is examined. The variation in gas volume fraction, $\varepsilon_G(t)$, with time, t, is assumed to fluctuate around a mean value, $\bar{\varepsilon}_G$, as follows:

$$\varepsilon_G(t) = \bar{\varepsilon}_G + \Delta\varepsilon_G \sin \omega t \quad \text{for } 0 \leqslant \omega t \leqslant 2\pi. \tag{21}$$

The measured intensity, I, with reference to the empty column intensity, I_0, is given by

$$\frac{I}{I_0} = \frac{1}{2\pi} \int_0^{2\pi/\omega} e^{-\mu\left(1-\bar{\varepsilon}_G-\Delta\varepsilon_G \sin \omega t\right)L} \omega \, dt \equiv e^{-\mu\left(1-\bar{\varepsilon}_G-\delta\varepsilon_G\right)L}, \tag{22}$$

where $\delta\varepsilon_G$ is defined to be the magnitude of the overestimation of $\bar{\varepsilon}_G$. Solving for $\delta\varepsilon_G$ yields

$$\delta\varepsilon_G = \frac{1}{\mu L} \ln\left(\frac{1}{2\pi} \int_0^{2\pi/\omega} e^{\mu\Delta\varepsilon_G L \sin \omega t} \omega \, dt\right) = \frac{1}{\mu L} \ln\left[\mathbf{I_0}(\mu L \Delta\varepsilon_G)\right] \cong \frac{1}{4}\mu L \Delta\varepsilon_G^2, \tag{23}$$

where $\mathbf{I_0}$ is the zeroth-order Bessel function. For water at the center of the column ($L = 19.05$ cm), if $\Delta\varepsilon_G = 0.16$, then $\delta\varepsilon_G = 0.01$. Thus, for an average gas volume fraction of 0.16, the gas volume fraction would have vary from 0 to 0.32 before the bias reaches a value of 0.01. Based on George et al. (2000), variations in volume fraction appear to be much less than this, suggesting that the bias is significantly less than the standard deviation of ± 0.01 found above for these measurements.

In addition to the mathematical analysis presented above, Torczynski et al. (1997) reported experiments in which GDT was compared to other techniques. First, average gas volume fractions calculated from integrating the GDT profiles over the cross-section were found to be in good agreement with values calculated from differential pressure measurements. Second, GDT measurements of phase-volume fractions in particle-laden liquids were found to be in good agreement with the known amount of suspended solids. Taken together, the above results suggest an uncertainty of ± 0.01 for the GDT technique.

George et al. (2000) provide an extensive discussion of the uncertainty associated with the EIT technique described above. In brief, several sources of uncertainty were identified and examined. First, the Maxwell–Hewitt relation (Eq. (12)), which is used to convert conductivity information into phase-volume-fraction information, is an approximation. Second, the voltages measured by the EIT system are inherently time-averaged, so the conductivity field returned by the reconstruction algorithm may differ from the time-averaged conductivity field. Third, a form for the spatial variation of the conductivity field is explicitly prescribed. Other sources of uncertainty include capacitive effects (the electrical response is taken to be purely resistive), the numerical accuracy of the voltage simulations in the reconstruction, and the accuracy of the voltage measurements themselves. George et al. (2000) identified the first two as the most significant sources of uncertainty.

George et al. (2000) provided extensive numerical simulations quantifying the accuracy of the Maxwell–Hewitt relation (Eq. (12)), which is used to convert electrical-conductivity information into phase-volume-fraction information. In brief, they performed a large number of two-dimensional and three-dimensional FEM simulations to determine the effective conductivity of

insulating inclusions in a medium of otherwise uniform conductivity. Their results showed that the Maxwell–Hewitt relation predicted an effective conductivity that was typically within about 0.01 of the computed effective conductivity so long as the inclusions do not overlap and completely block current flow. In fact, a close examination of the three-dimensional cases shown in Fig. 3 of George et al. (2000) indicates that an α value of 0.6, rather than the value of 0.5 used in the figure, would improve the agreement between the simulations and the Maxwell–Hewitt relation.

The use of time-averaged voltages in the reconstruction can also affect the accuracy of the EIT technique. The same model problem used to assess the effect of temporal averaging on GDT is examined to assess the effect of temporal averaging on EIT. The temporal variation of the gas volume fraction shown in Eq. (15), namely a sinusoidal oscillation with an amplitude of $\Delta\varepsilon_G$ about a mean value of $\bar{\varepsilon}_G$, is again considered. Using the facts that the measured voltages are inversely proportional to the electrical conductivity and that the conductivity is related to the gas volume fraction by the Maxwell–Hewitt relation, the gas-volume-fraction error $\delta\varepsilon_G$ (the difference between the apparent and true values of the time-averaged gas volume fraction) can be determined for this situation:

$$\delta\varepsilon_G = (1-\varepsilon_G) - \sqrt{(1-\varepsilon_G)^2 - (\Delta\varepsilon_G)^2} \approx (\Delta\varepsilon_G)^2/[2(1-\varepsilon_G)]. \tag{24}$$

Interestingly, the parameter α is absent from this equation. Thus, for an average gas volume fraction $\bar{\varepsilon}_G$ of 0.16 and a fluctuation $\Delta\varepsilon_G$ of 0.16 (i.e., a very large fluctuation with the gas volume fraction varying between 0 and 0.32), the gas-volume-fraction error $\delta\varepsilon_G$ is 0.015, which is comparable to the error introduced into GDT by time-averaging. As previously stated, based on measurements of volume-fraction fluctuations using a bulk-void-fraction meter (George et al., 2000), the variations in gas volume fraction appear to be much smaller than this.

George et al. (2000) provided several demonstrations of the quantitative performance of the EIT system. First, the high level of agreement achieved between computed and measured values for the "fundamental" voltage solution indicate that the combination of capacitive effects, numerical-accuracy issues, and voltage-measurement issues produces an uncertainty of well less than 1%. Second, reconstructions performed using numerically synthesized data were virtually indistinguishable from the conductivity field used to synthesize the data. Third, a series of double-blind experiments with insulating cylinders placed inside the electrode ring yielded excellent reconstructions of the location and diameter of the cylinder. Fourth, the EIT system was applied to a mixer-driven liquid–solid flow experiment and found to reproduce the known solid volume fraction to within 0.003 for average solid volume fractions up to 0.05. The particles used in these experiments are identical to those in some of the three-phase flows discussed in later sections. Fifth, a direct comparison of the GDT and EIT techniques for gas–liquid bubble-column flows indicated differences of 0.01 or less for the gas-volume-fraction radial profiles at all radial locations over a broad range of superficial gas velocities. The good agreement between GDT and EIT profiles suggests that the selected form of the conductivity profile does not affect the EIT reconstruction adversely. Taken in toto, these results suggest an uncertainty of ± 0.01 for EIT measurements of material-distribution profiles and an uncertainty of ± 0.02 for phase volume fractions from the combined GDT/EIT technique.

4. Results and discussion

4.1. Three-phase profiles

The first parameter investigated is superficial gas velocity. Figs. 7(a)–(d) show phase-volume-fraction profiles for four superficial gas velocities for the 170–260 μm polystyrene particles at a nominal slurry concentration, $\bar{\varepsilon}_S^{nom}$, of 0.10. Several general observations can be made about the results. First, as expected, the gas volume fraction increases as the superficial gas velocity is increased. The gas-volume-fraction profiles behave like those found in gas–liquid flows, which increase preferentially on the column axis as U_G is increased (Joshi et al., 1998). As expected, the profiles of ε_L decrease with increasing U_G as the liquid phase is displaced by the gas phase. The profiles of ε_S do not change significantly in magnitude as U_G increases with respect to the experimental uncertainty and are mostly flat with a slight increase at the walls. However, examining

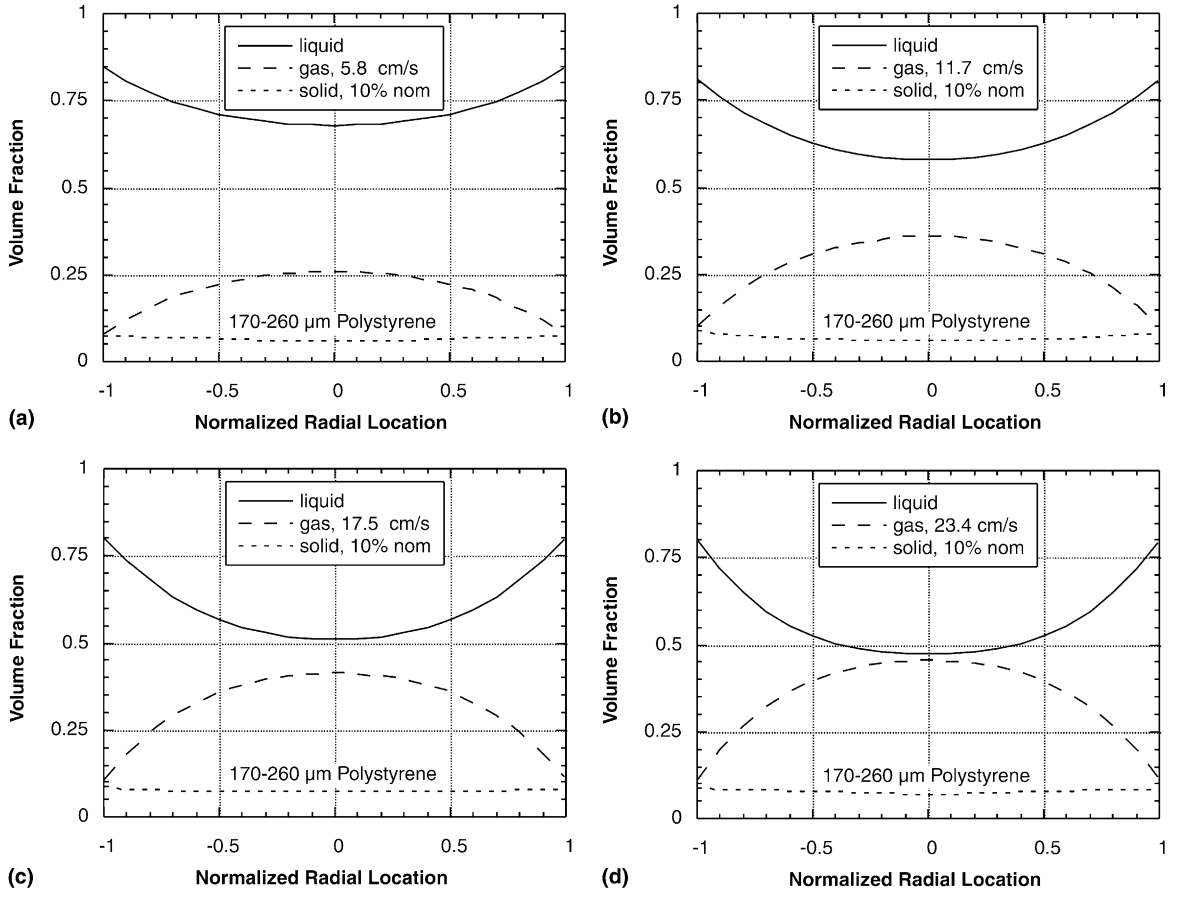

Fig. 7. (a)–(d). Phase-volume-fraction profiles as a function of superficial gas velocity: (a) 5.8 cm/s, (b) 11.7 cm/s, (c) 17.5 cm/s, and (d) 23.4 cm/s. The solid phase is 170–260 μm polystyrene particles at a nominal slurry concentration of 0.10.

solids profiles for all of the cases studied reveals profile shapes that include concave upward, concave downward, and a maximum at a radial location between the axis and the wall. In most cases these variations lie within or close to the indicated uncertainty and should not be considered significant.

The second parameter of interest is nominal slurry concentration, $\bar{\varepsilon}_S^{nom} = V_S/(V_S + V_L)$. Figs. 8(a)–(d) show phase-volume-fraction profiles at four different values of $\bar{\varepsilon}_S^{nom}$ for the 120–200 μm glass particles at a superficial gas velocity of 17.5 cm/s. As expected, the magnitude of the profiles of ε_S is seen to increase with nominal slurry concentration. The shape of the profiles of ε_S evolves from a maximum at a radial location between the axis and the wall to concave upward, but as noted above, these changes are within the indicated uncertainty and may not be significant. The shape and magnitude of the profiles of ε_G are almost identical in all four plots to within ±0.03. Indeed, for the polystyrene particles at each gas flow rate examined, the shape of the gas-volume-fraction radial profile is also unaffected by the addition of solids to within ±0.03 in volume

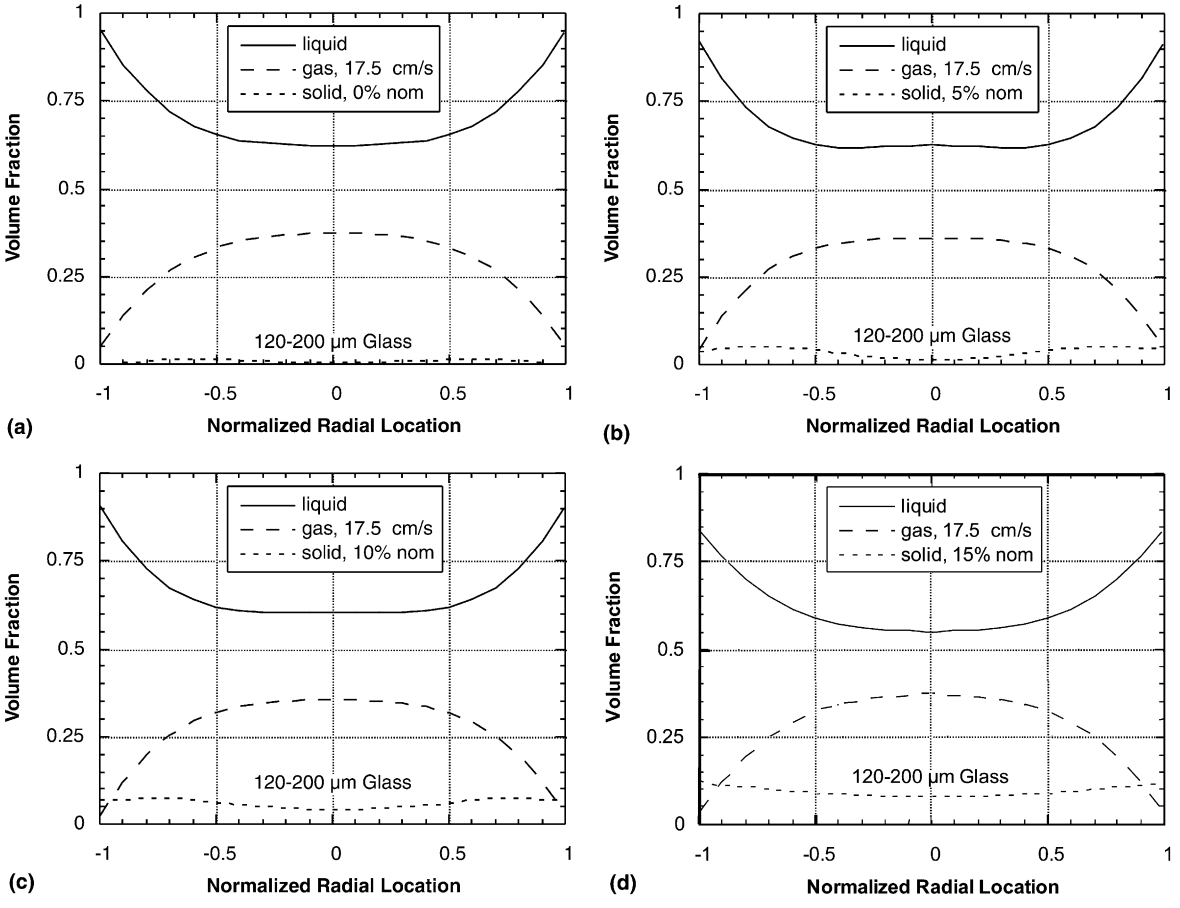

Fig. 8. (a)–(d). Phase-volume-fraction profiles as a function of nominal slurry concentration, $\bar{\varepsilon}_S^{nom}$: (a) 0.00, (b) 0.05, (c) 0.10, and (d) 0.15. The superficial gas velocity is 17.5 cm/s and the solid phase is 120–200 μm glass particles.

fraction. Finally, since ε_S increases while ε_G remains relatively constant as $\bar{\varepsilon}_S^{nom}$ is increased, ε_L decreases accordingly as the solid displaces the liquid.

The effect of particle density on the phase-volume-fraction profiles is observed by comparing results from the 170–260 μm polystyrene particles and from the more dense 120–200 μm glass particles. In general, Figs. 7(a)–(d) for the polystyrene particles show that the profiles of ε_G are rounded or parabolic in shape. Figs. 8(a)–(d) for the glass particles show that the profiles of ε_G are noticeably flatter at the center of the column or quartic in shape. These changes in profile shape are once again close to the experimental uncertainty. Furthermore, since water and polystyrene have similar attenuation coefficients, the gas-volume-fraction profiles for the polystyrene particles are determined mainly by GDT (Eq. (8)). However, water and glass have appreciably different attenuation coefficients and the gas-volume-fraction profiles for the glass particles are determined in a coupled fashion from the combined EIT and GDT measurements. In contrast to the above results, the profile shapes of the GDT function, $f_\mu(r)$, do not change noticeably for the two particle types. Thus, the changes in the profile shapes observed for the glass particles are caused by the EIT measurements.

The effect of particle size on phase-volume-fraction profiles can be examined for both particle types. Fig. 9 shows phase-volume-fraction profiles for which the solid phase is 40–100 μm glass particles with a superficial gas velocity of 17.5 cm/s and a nominal slurry concentration of 0.10. This figure can be compared to Fig. 8(c) for the 120–200 μm glass particles at the same flow conditions. All three of the profiles in these figures are very similar in shape. Fig. 10 shows phase-volume-fraction profiles for which the solid phase is 200–700 μm polystyrene particles, with a superficial gas velocity of 11.7 cm/s and a nominal slurry concentration of 0.10. This can be compared to Fig. 7(b) for the 170–260 μm polystyrene particles at the same flow conditions. Again, all of the profiles in these figures are very similar.

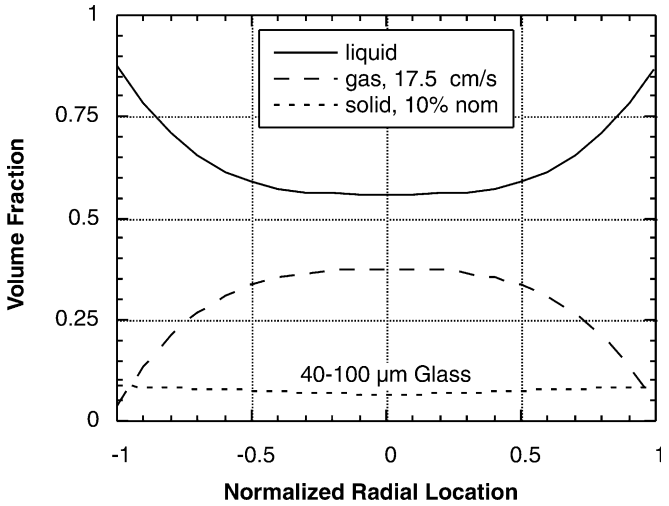

Fig. 9. Phase-volume-fraction profiles where the solid phase is 40–100 μm glass particles, the superficial gas velocity is 17.5 cm/s, and the nominal slurry concentration is 0.10.

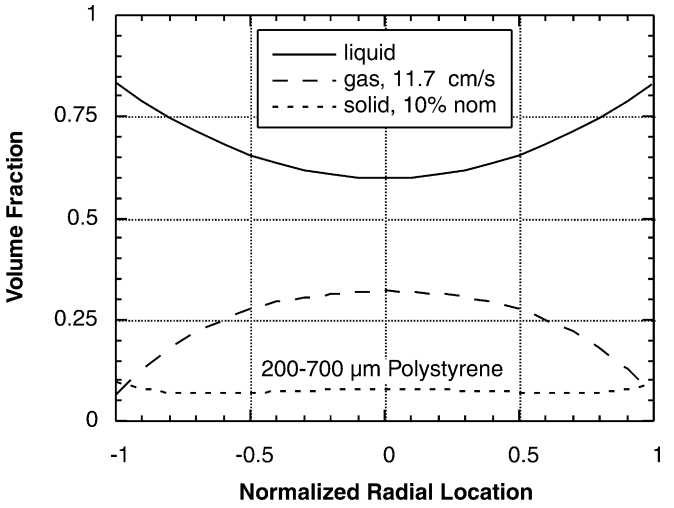

Fig. 10. Phase-volume-fraction profiles where the solid phase is 200-700 μm polystyrene particles, the superficial gas velocity is 11.7 cm/s, and the nominal slurry concentration is 0.10.

4.2. Cross-sectionally averaged volume fractions

Changes in the magnitudes between the profiles are sometimes hard to discern; to examine small changes, cross-sectionally averaged data are computed from the reconstructions by numerically integrating the profiles. One benefit of looking at the cross-sectionally averaged data is that more accurate results can be obtained for the averages than for the individually reconstructed data points (Mwambela et al., 1997).

As a validation of the combined GDT/EIT technique, the measured average slurry concentration, $\bar{\varepsilon}_S = \varepsilon_S/(\varepsilon_S + \varepsilon_L)$, can be compared to the nominal slurry concentration, $\bar{\varepsilon}_S^{nom} = V_S/(V_S + V_L)$. In a strongly mixed system there should be a roughly uniform distribution of the solid phase within the liquid phase along the height of the column. The measured slurry concentration, $\bar{\varepsilon}_S$, is determined by integrating the volume fraction profiles over the cross-section, and the nominal slurry concentration is determined from the known volumes of liquid and solid. Fig. 11 shows the measured slurry concentration as a function of the superficial gas velocity for all experiments. Several observations can be made about this figure. First, for cases where $\bar{\varepsilon}_S^{nom} = 0$, $\bar{\varepsilon}_S$ is found to be less than 0.01 for superficial gas velocities less than about 10 cm/s and less than 0.03 for higher velocities. Thus, there is a slight bias in the slurry concentration at higher gas velocities. However, this bias has almost no effect on the measured gas volume fraction for the cases with polystyrene particles because the attenuation coefficients for the solid and the liquid phases are almost the same (see Eq. (8)). The effect of this bias on the gas volume fractions for the cases with glass particles is uncertain. Second, for the polystyrene-particle cases with nominal slurry concentrations from 0.05 to 0.30, $\bar{\varepsilon}_S$ approaches $\bar{\varepsilon}_S^{nom}$ and then slightly exceeds it as the superficial gas velocity increases. It is likely that the overprediction results from the bias observed above when solids are absent. Third, for the cases with glass particles, the measured slurry concentrations are generally lower than those for the polystyrene particles, particularly at the higher nominal slurry concentrations. Also, as the glass particle size increases, the measured slurry

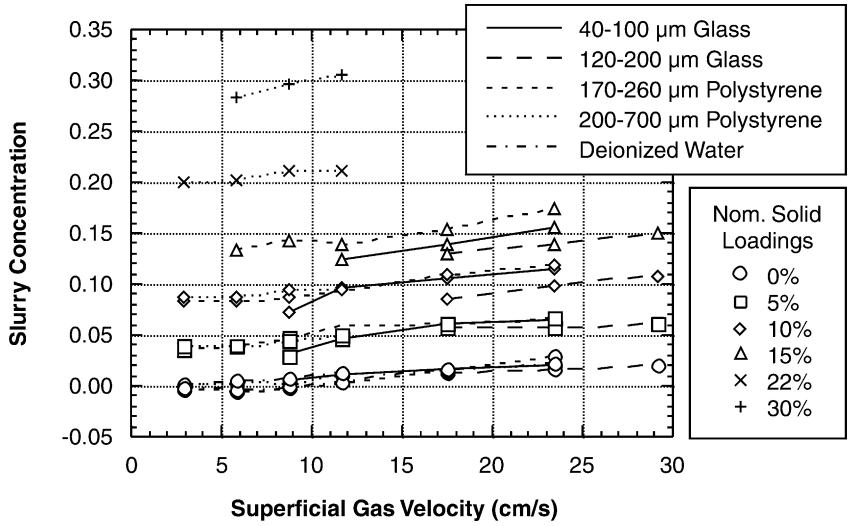

Fig. 11. Comparison of nominal slurry concentration, $\bar{\varepsilon}_S^{nom}$, and slurry concentration at measurement plane from combined GDT/EIT measurements.

concentration decreases. The reduced slurry concentrations probably result from incomplete lofting of the higher-density glass particles, which worsens with particle size. Based on these results, it is concluded that the combined GDT/EIT technique reasonably predicts slurry concentrations for these experiments to an accuracy of approximately ± 0.03. This cumulative error corresponds correctly to the individual error for each technique of ± 0.01 presented previously.

The effect of the presence of solids on the average gas volume fraction, $\bar{\varepsilon}_G$, is quantified in Table 2 and in Fig. 12, which show $\bar{\varepsilon}_G$ as a function of superficial gas velocity, U_G, for all four particle

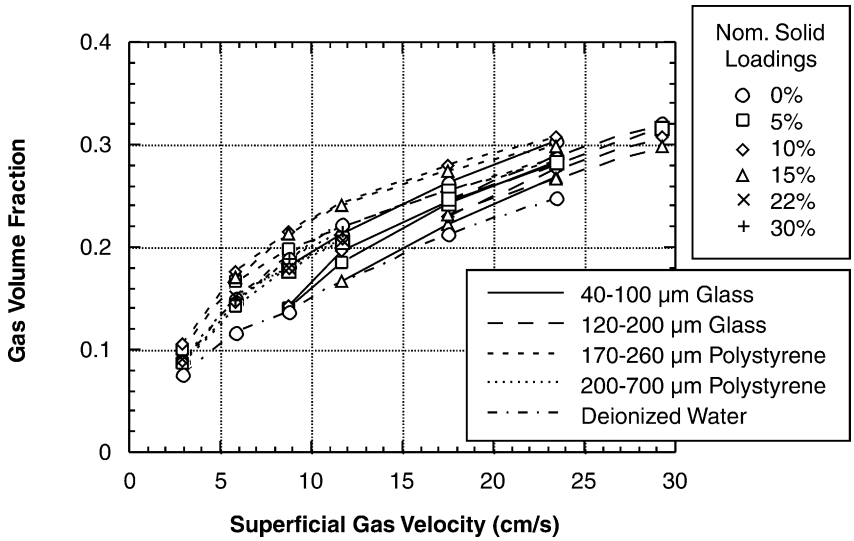

Fig. 12. Cross-sectionally averaged gas volume fraction as a function of superficial gas velocity.

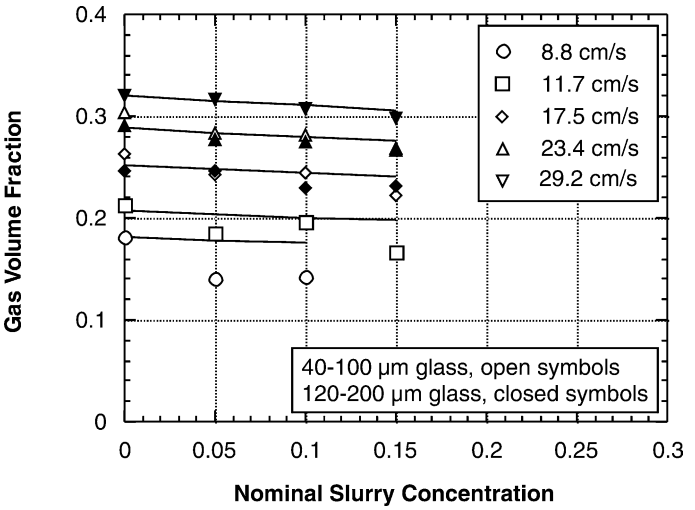

Fig. 13. Gas volume fraction as a function of nominal slurry concentration, $\bar{\varepsilon}_S^{nom}$, for glass particles: 40–100 μm particles are open symbols and the 120–200 μm particles are closed symbols. The solid lines are the correlation of Eq. (30).

types. For comparison, Fig. 12 also shows average gas volume fractions obtained using clean, deionized water and no solids. In all cases $\bar{\varepsilon}_G$ is seen to increase monotonically with U_G, as expected. A nominal solid volume fraction of 0% in these graphs indicates cases in which particles loaded for previous experiments have been removed from the water, leaving particle surface coating material behind in the water. These gas volume fractions are considerably lower than for the cases in which particles are employed, but all results can be described to within ± 0.04 by a curve passing through the middle of the data. As noted earlier, the addition of particles also unavoidably adds surfactants that reduce surface tension and change the gas volume fraction, $\bar{\varepsilon}_G$, by $+0.02$ to $+0.06$, substantially more than the change produced by the particles themselves.

In order to see the effects of particle diameter and density more clearly, the data in Fig. 12 are plotted separately in Figs. 13 and 14 for each particle type as a function of nominal slurry concentration. The average gas volume fractions in these experiments are roughly independent of particle diameter for the glass particles (Fig. 13). However, for the 170–260 μm polystyrene particles, increases in $\bar{\varepsilon}_G$ of up to 0.04 are observed for nominal slurry concentrations greater than 0.05 (see Fig. 14). Decreases in $\bar{\varepsilon}_G$ with increasing solids density are also evident from these experiments. The plot for glass particles (Fig. 13) shows a clear decrease in gas volume fraction (by as much as 0.04 in $\bar{\varepsilon}_G$) with increasing solid volume fraction, but no such trend is observed for the polystyrene particles (Fig. 14).

4.3. Average gas-volume-fraction correlation

Typically, average gas-volume-fraction measurements in bubble-column flows are correlated using three liquid properties: density, viscosity, and surface tension. Greater liquid density increases the buoyant force on a bubble, which increases its velocity relative to the liquid and thereby tends to decrease the gas volume fraction. However, greater liquid density also increases

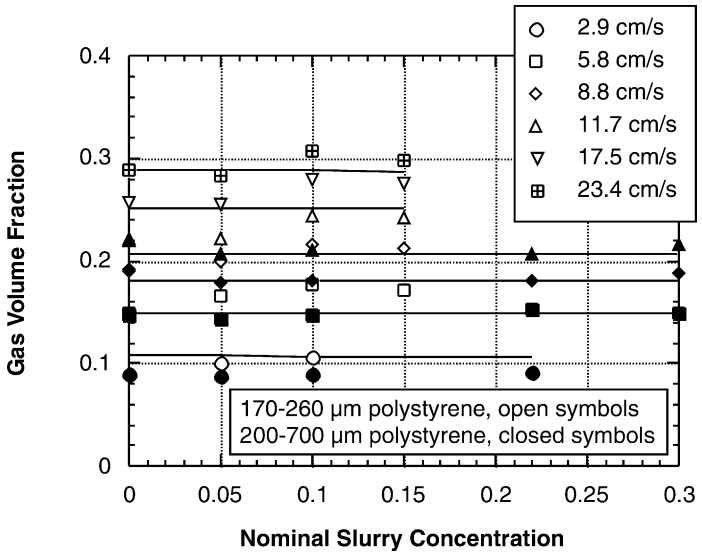

Fig. 14. Gas volume fraction as a function of nominal slurry concentration, $\bar{\varepsilon}_S^{nom}$, for polystyrene particles: 170–260 μm particles are open symbols and the 200–700 μm particles are closed symbols. The solid lines are the correlation of Eq. (30).

its inertia, which enhances bubble breakup, reduces bubble size and velocity relative to the liquid, and thereby tends to increase the gas volume fraction. A majority of the empirical gas–liquid correlations in the exhaustive review by Joshi et al. (1998) indicate that increasing liquid density generally increases gas volume fraction. This suggests that the bubble-breakup effect of the liquid density tends to dominate in bubble columns. Similarly greater liquid viscosity decreases bubble velocity but increases bubble size; in this case the latter effect dominates, and the net result is generally a reduction in gas volume fraction. Finally, greater surface tension generally increases bubble size and thereby reduces gas volume fraction. These trends with liquid properties are represented in empirical correlations of gas volume fraction in terms of the density ratio ρ_L/ρ_G and the Morton, Weber, and Reynolds numbers, which can be defined respectively as follows:

$$Mo = \frac{g\eta_L^4(\rho_L - \rho_G)}{\rho_L^2\sigma^3}, \tag{25}$$

$$We = \frac{U_G^2 D\rho_L}{\sigma}, \tag{26}$$

$$Re = \frac{U_G D\rho_L}{\eta_L}, \tag{27}$$

where ρ_L is the liquid density, ρ_G is the gas density, η_L is the liquid absolute viscosity, σ is the surface tension (not to be confused with the electrical conductivity), D is the column diameter, and g is the gravitational acceleration.

One way to correlate the three-phase data presented in this paper is to assume that the solid is uniformly dispersed in the liquid and that the slurry behaves as a single phase with the properties of the suspension. The effective density can be calculated as

$$\rho = \bar{\varepsilon}_S^{nom}\rho_S + \left(1 - \bar{\varepsilon}_S^{nom}\right)\rho_L, \tag{28}$$

where ρ_S is the solid density. The effective viscosity can be calculated using a correlation for a suspension from Thomas (1965) as

$$\frac{\eta}{\eta_L} = 1 + 2.5\bar{\varepsilon}_S^{nom} + 10.05\bar{\varepsilon}_S^{nom^2} + 0.00273\exp\left(16.6\bar{\varepsilon}_S^{nom}\right). \tag{29}$$

This correlation does not account for particle size, assumes a uniform size distribution of particles, and is valid for particle volume fractions up to 0.25. The changes in surface tension are much harder to account for, so the surface tension of the electrolyte solution is measured for each experiment and found to decrease by 2–20 dyn/cm from the surface tension of pure water. A strictly empirical correlation based on a nondimensional analysis is used to fit the experimental data in Figs. 13 and 14,

$$\bar{\varepsilon}_G = CMo^{m_1}\left(\frac{\rho_G}{\rho}\right)^{m_2}\left(\frac{We}{Re}\right)^{m_3}, \tag{30}$$

where $C = 2.1,\ m_1 = -0.12,\ m_2 = 0.35$, and $m_3 = 0.48$. Note that the use of (We/Re) removes the dependency on column diameter, as is believed to be appropriate for large-diameter systems by some researchers (Wilkinson et al., 1992). The correlation curves are also shown in Figs. 13 and 14. For the glass particles (Fig. 13), the correlation generally reproduces the data except at the lowest superficial gas velocity. Also, the data from the 200–700 μm polystyrene particles (Fig. 14) show good agreement with the correlation. However, the data from the experiments with 170–260 μm polystyrene particles are not described accurately by the correlation.

5. Conclusions

The application of tomographic techniques to multiphase flows continues to be a significant research topic for which goals include improvements in temporal and spatial resolution, quantitative accuracy, and applicability to a broader class of multiphase flows. To these ends, a GDT system and an EIT system, developed collaboratively by Sandia National Laboratories and the University of Michigan, have been combined to measure three-phase volume fractions in vertical flows. The study employs solid phases with conductive properties similar to air but densities similar to water, so that each of the three phases has a unique combination of attenuating and conductive properties. This approach also requires that the constitutive equations for both measurement methods be solved simultaneously to determine the distributions of all three phases.

Experiments with solid particles of different sizes and densities are performed to determine the influences of these quantities on phase-volume-fraction profiles. Four particle types are examined: 40–100 μm and 120–200 μm glass particles (2.41 g/cm^3), and 170–260 μm and 200–700 μm

polystyrene particles (1.04 g/cm^3). Nominal slurry concentrations, $\bar{\varepsilon}_S^{nom} = V_S/(V_S + V_L)$, of up to 0.30 are examined for superficial gas velocities in the 2–30 cm/s range.

Over the range of nominal slurry concentrations, the gas distribution for each gas flow rate is relatively insensitive to the amount of solids present in the mixture. For all of the particle types examined, a maximum variation in gas volume fraction of ± 0.04 is observed for a given superficial gas velocity. The neutrally buoyant 200–700 μm polystyrene particles are found to have almost no effect on the gas distribution. A slight increase in gas volume fraction with nominal slurry concentration is observed for the 170–260 μm polystyrene particles. No particle size effect concentration is observed for the glass particles. A slight decrease in gas volume fraction with nominal slurry concentration is observed with the glass particles, which are substantially more dense than the liquid. The physical mechanism responsible for this effect is not yet clear. By comparison, surface-tension changes from contaminants added with the particles are more important than changes from the presence of the particles themselves. Finally, the particles appear to be approximately uniformly distributed in the liquid, but difficulty in lofting higher-density particles is observed.

With the successful combination of EIT and GDT reported here, additional investigations are now possible to help develop phase-interaction models for three-phase bubble-columns. Future efforts will focus on extending the EIT technique to Sandia's 48-cm diameter slurry bubble-column reactor (SBCR) testbed and to other industrial-scale systems. Further modifications might also include extending the resistive electrical technique to a capacitive technique that would increase the number of choices for each phase (for example, a nonconducting fluid).

Acknowledgements

This work was performed at Sandia National Laboratories. Sandia is a multiprogram laboratory operated by Sandia Corporation, a Lockheed Martin Company, for the United States Department of Energy under Contract DE-AC04-94AL85000. A portion of this work was funded by the National Energy Technology Laboratory under Field Work Proposal FEW-8616. The authors are grateful for technical interactions with B.A. Toseland of Air Products and Chemicals, Inc. The authors would also like to thank C.B. Lafferty and W.C. Ginn for their skilled technical assistance, D.R. Adkins for his early work with the GDT system, A.T. Leger for her early work with the EIT system, R.R. Lagasse for performing particle size analysis, and N.B. Jackson for her technical discussions related to catalysis.

References

Ceccio, S.L., George, D.L., 1996. A review of electrical impedance techniques for the measurement of multiphase flows. J. Fluids Eng. 118, 391–399.

Dickin, F.J., Williams, R.A., Beck, M.S., 1993. Determination of composition and motion of multicomponent mixtures in process vessels using electrical impedance tomography – I. Principles and process engineering applications. Chem. Eng. Sci. 48, 1883–1897.

George, D.L., Ceccio, S.L., O'Hern, T.J., Shollenberger, K.A., Torczynski, J.R., 1998a. Advanced material distribution measurement in multiphase flows: a case study. Proceedings of the 1998 ASME International Mechanical Engineering Conference and Exposition, ASME, FED 247, 31–42.

George, D.L., Ceccio, S.L., Shollenberger, K.A., Torczynski, J.R., O'Hern, T.J., 1998b. Comparison of electrical-impedance tomography and gamma-densitometry tomography for the measurement of gas volume fraction profiles in a bubble column. In: Proceedings of the 1998 ASME Fluids Engineering Division Summer Meeting, FED, vol. 245. No. 98-5081.

George, D.L., Torczynski, J.R., Shollenberger, K.A., O'Hern, T.J., Ceccio, S.L., 2000. Validation of electrical-impedance tomography for measurements of material distribution in two-phase flows. Int. J. Multiphase Flow 26, 549–581.

Hewitt, G.F., 1978. Measurement of Two-Phase Flow Parameters. Academic Press, London.

Jackson, N.B., Torczynski, J.R., Shollenberger, K.A., O'Hern, T.J., Adkins, D.R., 1996. Hydrodynamic characterization of slurry bubble-column reactors for Fischer–Tropsch synthesis. In: Proceedings of the Thirteenth Annual International Pittsburgh Coal Conference, vol. 2: Coal-Energy and the Environment. pp. 1226–1231.

Jones, O.C., Lin, J.-T., Ovacik, L., 1992. Investigation of electrical impedance imaging relative to two-phase, gas–liquid flows. Chem. Eng. Comm. 118, 299–325.

Jones, O.C., Lin, J.-T., Ovacik, L., Shu, H., 1993. Impedance imaging relative to gas–liquid systems. Nucl. Eng. Design 141, 159–176.

Jones, O.C., Lin, J.T., Shu, H., Ovacik, L., He, Y., 1994. Impedance imaging relative to binary mixtures. In: Fifth International Symposium on Liquid–Solid Flows, ASME.

Joshi, J.B., Parasu Veera, U., Prasad, Ch.V., Phanikumar, D.V., Deshphande, N.S., Thakre, S.S., Thorat, B.N., 1998. Gas hold-up structure in bubble column reactors. PINSA 64A (4), 441–567.

Kumar, S.B., Moslemian, D., Dudukovic, M.P., 1995. A gamma-ray tomographic scanner for imaging voidage distribution in 2-phase flow systems. Flow Meas. Instrum. 6, 61–73.

Lamarsh, J.R., 1983. Introduction to Nuclear Engineering. Addison-Wesley, Reading, MA, pp. 78–88, 472–488, 648–649.

Maxwell, J.C., 1881. A Treatise on Electricity and Magnetism. Clarendon Press, Oxford.

Mwambela, A.J., Kirkedam, E., Johansen, G.A., Isaksen, O., 1997. Reconstruction of capacitance tomography data using global entropic thresholding methods: experimental validation. In: Frontiers in Industrial Process Tomography II, Proceedings of Engineering Foundation Conference.

O'Hern, T.J., Torczynski, J.R., Ceccio, S.L., Tassin, A.L., Chahine, G.L., Duraiswami, R., Sarkar, K., 1995. Development of an electrical-impedance tomography system for an air–water vertical bubble column. ASME Forum on Measurement Techniques in Multiphase Flows, FED 233, 531–537.

Plaskowski, A., Beck, M.S., Thorn, R., Dyakowski, T., 1995. Imaging Industrial Flows: Applications of Electrical Process Tomography. Institute of Physics Publishing, Bristol, England.

Shah, Y.T., Deckwer, W.D., 1983. Handbook of Fluids in Motion: Hydrodynamics of Bubble Columns. Ann Arbor Science Publishers, Ann Arbor, MI, pp. 583–620.

Shollenberger, K.A., Torczynski, J.R., Adkins, D.R., O'Hern, T.J., Jackson, N.B., 1997a. Gamma-densitometry tomography of gas holdup spatial distribution in industrial-scale bubble columns. Chem. Eng. Sci. 52, 2037–2048.

Shollenberger, K.A., Torczynski, J.R, O'Hern, T.J., Adkins, D.R., Ceccio, S.L., George, D.L., 1997b. Comparison of gamma-densitometry tomography and electrical-impedance tomography for determining material distribution in liquid–solid flows. In: Proceedings of the 1997 ASME Fluids Engineering Division Summer Meeting, vol. FEDSM '97. No. 97-3690.

Somersalo, E., Cheney, M., Isaacson, D., 1992. Existence and uniqueness for electrode models for electric current computed tomography. SIAM J. Appl. Math. 52, 1023–1040.

Thomas, D.G., 1965. Transport characteristics of suspension: VIII. A note on the viscosity of Newtonian suspensions of uniform spherical particles. J. Colloid Sci. 20, 267–277.

Thoraeus, R., 1965. Attenuation of gamma radiation from ^{60}Co, ^{137}Cs, ^{192}Ir, and ^{226}Ra in various materials used in radiology. Acta Radiologica 3, 81–86.

Torczynski, J.R., O'Hern, T.J., Shollenberger, K.A., Ceccio, S.L., Tassin, A.L., 1996a. Finite element method electrical-impedance tomography for phase distribution determination in multiphase flows: validation calculations and experiments. ASME Cavitation and Multiphase Flow Forum, FED 236, 497–501.

Torczynski, J.R., Adkins, D.R., Shollenberger, K.A., O'Hern, T.J., 1996b. Application of gamma-densitometry tomography to determine phase spatial variation in two-phase and three-phase bubbly flows. ASME Cavitation and Multiphase Flow Forum, FED 236, 503–508.

Torczynski, J.R., O'Hern, T.J., Adkins, D.R., Jackson, N.B., Shollenberger, K.A., 1997. Advanced Tomographic Flow Diagnostics for Opaque Multiphase Fluids. Report SAND97-1176, Sandia National Laboratories, Albuquerque, NM.

Vest, C.M., 1985. Tomography for properties of materials that bend rays: a tutorial. Appl. Opt. 24, 4089–4094.

Wilkinson, P.M., Spek, A.P., van Dierendonck, L.L., 1992. Design parameters estimation for scale-up of high-pressure bubble columns. AIChE J. 38 (4), 544–554.

Yorkey, T.J., Webster, J.G., Tompkins, W.J., 1987. Comparing reconstruction methods for electrical impedance tomography. IEEE Trans. Biomedical Eng. 11, 843–852.